

1
2
3
4
5
6
7
8
9
10
11
12
13
14
15

Accuracy and Resolution of SWOT Altimetry: Foundation Seamounts

Y. Yu¹, D. T. Sandwell¹, G. Dibarboure², C. Chen³, and J. Wang³

¹Scripps Institution of Oceanography, University of California San Diego, La Jolla, USA.

²Centre National d'Etudes Spatiales, Toulouse, France.

³Jet Propulsion Laboratory, California Institute of Technology, Pasadena, USA.

Corresponding author: Yao Yu (yayu@ucsd.edu)

Key Points:

- A single cycle of SWOT at a typical significant wave height of 4 km, has a precision of 2.6 μ rad and a spatial resolution of 14 km.
- A stack of ~60 cycles of SWOT data provides a significant improvement in precision to ~1.2 μ rad and spatial resolution ~8 km.
- The accuracy and resolution of the marine gravity field derived from SWOT will exceed current models after 8 months.

16 **Abstract**

17 We assess the accuracy and spatial resolution of the Surface Water and Ocean Topography
18 (SWOT) swath altimeter for measuring marine gravity anomalies. The analysis is performed at
19 the Foundation Seamounts in the South Pacific where we developed a highly accurate gravity
20 field by combining the long-wavelength (> 40 km) gravity field derived from previous nadir
21 altimeters with the shorter wavelength gravity field from the seafloor topography as constrained
22 by the ship gravity. In this region, the slope of the ocean variability is 50-100 times smaller than
23 the gravity/slope signal of the seamounts so can be ignored in the analysis. Each SWOT cycle
24 can deliver gravity anomaly/SSS with an accuracy of $2.6 \text{ mGal}/\mu\text{rad}$ and a spatial resolution of
25 14 km, with accuracy diminishing when significant wave height (SWH) exceeds ~ 6 meters.
26 Averaging repeated SWOT measurements improves the accuracy and resolution. For example,
27 we expect that averaging just 10 repeats (7 months) results in accuracy/resolution that matches
28 the best marine gravity maps based on 230 months of nadir altimetry. With a mission lasting
29 over a year, SWOT promises a substantial leap in marine gravity accuracy and resolution,
30 uncovering previously uncharted details of the seafloor, including thousands of uncharted
31 seamounts.

32

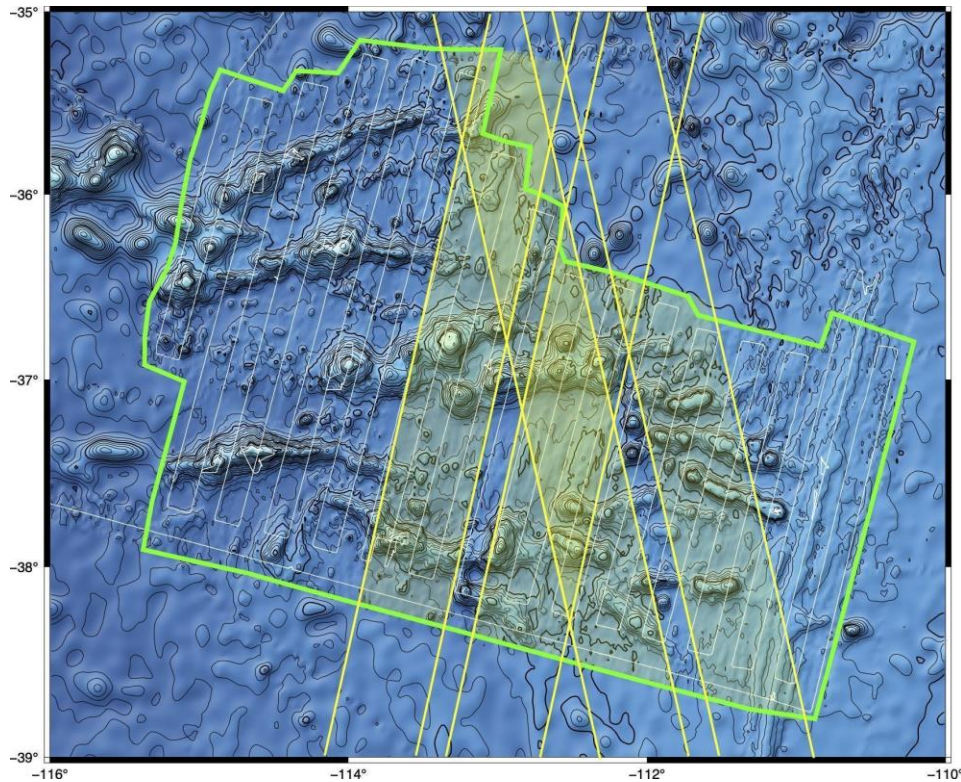
33 **Plain Language Summary**

34 The Surface Water and Ocean Topography (SWOT) is a satellite mission designed to measure
35 Earth's water body heights in wide-swath, offering opportunities to measure the ocean surface in
36 unprecedented details. This capability brings valuable high-resolution information about the
37 gravity field and seafloor underneath the ocean. This study aims to evaluate SWOT's
38 performance and our test area is in the South Pacific Ocean where we already know the ocean
39 topography and gravity field well. Results show that with SWOT global measurements lasting
40 over one year, it promises a significant improvement in uncharted details of the seafloor.

41

42 **1 Introduction**

43 The Foundation Seamounts is a 1400-km long chain of approximately 40 large seamounts
44 (2-4 km tall) constructed on young seafloor discovered by a combination of sparse ship
45 soundings and satellite altimeter-derived gravity (Mammericks, 1992). They were named the
46 Foundation Seamounts to acknowledge the contribution of the National Science Foundation to
47 the exploration of the Pacific Ocean. Since their discovery using sparse data, there have been
48 two major mapping and sampling cruises to these seamounts. In February-March 1995 the
49 German research vessel *Sonne* undertook a geological study of the Foundation Seamount Chain
50 (Devey et al., 1995). The aim of the cruise was to map and sample the chain in order to collect
51 geological and geophysical data on its evolution and its interaction with the Pacific-Antarctic
52 Ridge (PAR) spreading axis. In January-February, 1997 a more extensive multibeam and gravity
53 survey was carried out by the *L'Atalante* using a dual multibeam sonar and shipboard
54 gravimeter with a track spacing of 14 km to obtain nearly full bathymetry coverage (Figure 1).



55

56

57 **Figure 1.** Contours of seafloor topography of the Foundation Seamounts. White lines show ship
 58 tracks where gravity and multibeam bathymetry was collected. Green line shows perimeter of
 59 multibeam coverage. Yellow polygons with shading mark the swaths of the SWOT altimeter.

60

61 These seamounts have some unique characteristics that make it an ideal location for validation
 62 of SWOT measurements of sea surface height (SSH) and sea surface slope (SSS):

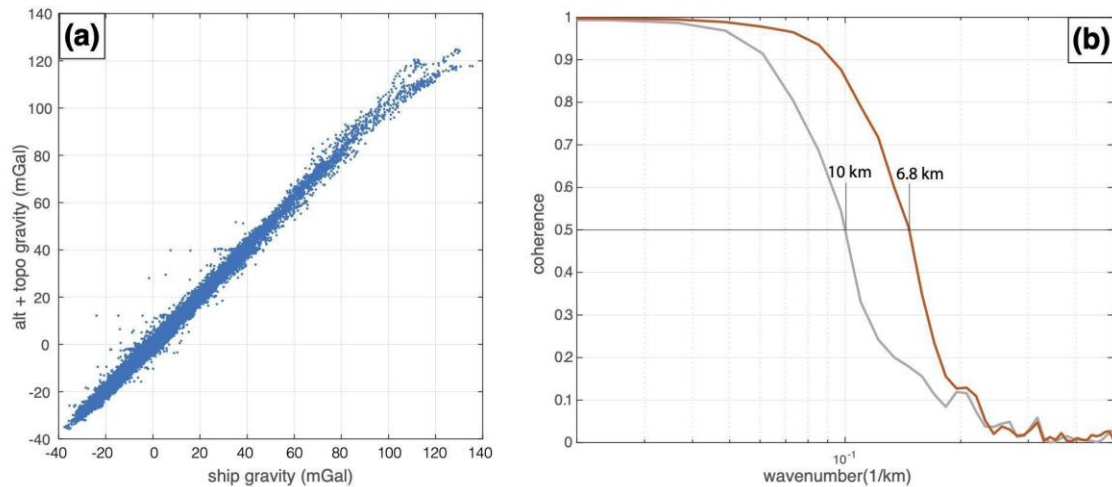
63 1) The seamounts formed on very young seafloor with age ranging from 0 to 9 Ma so the mean
 64 ocean depth varies from 2600 m to 3500 m. Compared to similar seamounts formed on typical
 65 ocean lithosphere, where the mean ocean depth is 4500 m, this shallow average depth in the
 66 Foundation Seamounts area results in a factor of $\exp(-2\pi\Delta d/\lambda) = 4.5$ times lower
 67 attenuation of the short-wavelength (~ 6 km) gravity field (where $\Delta d = -1450$ m and $\lambda = 6$
 68 km). Therefore, the short wavelength gravity signal at the sea surface is relatively large.

69 2) Because the seafloor is young and far from sources of sediment supply, it is mostly barren
 70 rock having a relative uniform density of 2550 to 2750 kg m^{-3} (Maia and Arkani-Hamed,
 71 2002). In addition, the seamounts are nearly locally compensated by very thin elastic plates
 72 (1-4 km). This results in a relatively uniform gravity to topography ratio at wavelengths less
 73 than about 60 km.

74 3) Within the areas of the 1-day SWOT coverage there are approximately 30 closely-spaced
 75 volcanic edifices having heights ranging from 1500 to 3500 m. These produce gravity peaks
 76 with very large amplitudes (20-120 mGal) and short wavelengths (Figure 2 and Figure S1).
 77 The accuracy of the shipboard gravity is better than 1 mGal so the signal to noise ratio
 78 exceeds 100.

79 4) The short wavelength (>16 km) SSS variability in the region is relatively low (e.g., SSS
 80 variability of $\sim 2 \mu\text{rad}$ in the observation of radar altimeter along-track profiles ($1 \mu\text{rad} = 10^{-6}$

81 which corresponds to ~ 1 mGal) (Yu et al., 2023). The uncertainty in the mean slope is
 82 between 0.5 and 2 μ rad depending on the number of repeat altimeter profiles. This
 83 oceanographic “noise” is 50-100 times smaller than the gravity signal so can be largely
 84 ignored in our analysis of SWOT data.



85
 86
 87 **Figure 2.** (a) Combined model gravity anomaly versus shipboard gravity (mean difference 0.215
 88 mGal, median absolute deviation 1.42 mGal). (b) (grey) Coherence between altimeter-only
 89 gravity and shipboard gravity falls to 0.5 at a wavelength of 10 km. (red) Coherence between
 90 combined gravity and ship gravity falls to 0.5 at a wavelength of 6.8 km. There is some coherent
 91 signal at 5.5 km wavelength so a sampling spacing should be 2.7 km or smaller.

92
 93 The objective of this paper is to assess the accuracy and resolution of SWOT altimetry (Fu et
 94 al., 2009; Morrow et al., 2019), focusing on measuring static geoid signals. We analyze the Level
 95 2 KaRIn Low Rate Sea Surface Height Data Product, Version 1.1 (also referred as the beta pre-
 96 validated version) (SWOT, 2023a) in the 1-day repeat orbit, in conjunction with the Level 3 low
 97 resolution SSH products (Dibarboure et al., 2023). To achieve this objective, we need a reference
 98 grid of mean sea surface (MSS – approximately the geoid) height or slope that is at least as
 99 accurate as the SWOT data. Current MSS and SSS grids are accurate to a few cm and a few μ rad,
 100 respectively (Schaeffer et al., 2023). Moreover, the altimeter-based grids cannot resolve
 101 wavelengths less than about 16 km because the data are filtered to reduce the noise from ocean
 102 waves and other environmental factors. Preliminary results of SWOT sea surface anomaly show
 103 residual gravity signals down to 8 km so the current best MSS grids (e.g.,
 104 MSS_CNES_CLS2022 and SIO_V32) constructed by traditional nadir altimetry are inadequate
 105 (Schaeffer et al., 2023; Sandwell et al., 2023) ([https://swotst.aviso.altimetry.fr/programs/2023-
 106 swot-st-program](https://swotst.aviso.altimetry.fr/programs/2023-swot-st-program)).

107
 108 Higher accuracy and resolution MSS/SSS can be achieved at the Foundation Seamounts using
 109 a combination of multibeam sonar and gravity collected over this area. Yu et al. (2021) proposed
 110 a similar analysis for the evaluation of the SWOT data in the South China Sea. The basic
 111 approach is to constrain the longer wavelength SSS (> 40 km) with the altimeter-derived
 112 products, and the shorter wavelength SSS (< 40 km) using the multibeam sonar bathymetry as

113 input to a 3-D isostatically compensated gravity model which includes sea surface gradient as
114 output. Details of the analysis are presented in the Supplementary Material. The important
115 parameter is the crustal density and this is adjusted so the combined gravity model best matches
116 the gravity profile observed by the ship.

117
118 Then we will compare the SWOT data collected over the Foundation Seamounts, to the SSS
119 grids (aka, model grids). We first compare the along- and across-track slope grids from SWOT,
120 with the corresponding east and north model slopes projected into the along- and cross-track
121 directions. This analysis reveals the slope noise (including both instrument noise and ocean
122 dynamics) for single passes of SWOT data. In addition, this analysis reveals the magnitude of the
123 SWOT interferometer roll errors that are shown as a smooth but large amplitude cross-swath
124 slope (SWOT, 2017). Further analysis shows that the SWOT slope noise depends strongly on the
125 significant wave height (SWH) and the distance to the central nadir, as predicted by the pre-
126 launch assessment (SWOT, 2017), albeit with much smaller amplitude. We then average, or
127 stack, many repeats of SWOT data to determine how the SSS noise improves as the number in
128 the stack increases. Finally, we perform a cross spectral analysis of the along-track slopes of
129 SWOT to the model slopes and establish the spatial resolution of the SWOT data for a single
130 pass as well as the stack. The results of the analysis provide information on how to best process
131 2 km resolution SWOT data for use in the recovery of short-wavelength SSS models and gravity
132 anomalies. The analysis also informs the physical oceanographic community on the smallest
133 resolvable ocean dynamic signals versus their wavelength in the presence of environmental
134 noise.

135

136 **2 Methods**

137 Our analysis begins with the level-2 beta pre-validated version, low resolution, expert
138 (L2_LR_SSH_Expert) data produced by the SWOT project (SWOT, 2023a). Data are provided
139 as passes that extend $\frac{1}{2}$ of an orbit either running from southwest to northeast (ascending) or
140 northwest to southeast (descending). The swath data are stored on a 2 km by 2 km grid with cells
141 oriented in the along-track (a) and cross-track directions (c). We create a corrected SSH as SSH
142 = $ssh_karin + mean_sea_surface_cnescls + height_cor_xover$. ssh_karin is the sea surface
143 height anomaly from the KaRIn measurement, with solid earth tide, ocean tide, coherent internal
144 tide, pole tide, and dynamic atmospheric correction applied. $mean_sea_surface_cnescls$ is the
145 CNES_CLS_15 mean sea surface height above the WGS84 reference ellipsoid. This mean sea
146 surface model lacks short-wavelength (~ 20 km) resolution compared to more recent ones (e.g.,
147 CNES_CLS_22) but is the current embedded reference in the SWOT L2 product (Schaeffer et
148 al., 2023). We apply the built-in crossover calibration by adding $height_cor_xover$ to the height.
149 These variable names are documented in the L2_LR_SSH_Expert netcdf files as well as the
150 corresponding documentation (SWOT, 2023b). Bad data are optionally eliminated using the flag
151 ssh_karin_qual .

152

153 In addition to the SWOT KaRIn data, we use global grids of east and north deflection of the
154 vertical based on traditional altimetry (Sandwell et al., 2021). The latest version V32 of these
155 grids are available at https://topex.ucsd.edu/pub/global_grav_1min/. The accuracy of these
156 vertical deflection grids is improved using the multibeam bathymetry data as described in the
157 Supplementary Material. The accuracy of the model east and north grids is $\sim 1.96 \mu\text{rad}$ based on

158 the comparison with ship gravity (Figure 2a) and the resolution is 6.8 km based on the cross-
 159 spectral coherence between the ship gravity and the gravity from the transformed model slope
 160 grids.

161
 162 Two passes of SWOT data (011 and 026) from the 1-day repeat orbit are windowed in an area
 163 of the Foundation seamounts (-116° to -110° longitude, and -39° to -35° latitude). There are ~90
 164 cycles in each pass that enable the analysis of single cycles or stacks (averages) of up to 90
 165 cycles. We are interested in the SSS so we take the gradient of the SSH data for each cycle in
 166 both passes. This results in 2-D grids of along-track and cross track slope. We then use the
 167 pyGMT command *grdtrack* to sample the model east and north slope grids at the same locations
 168 as the windowed SWOT grids. We project the north and east model grids into the directions of
 169 the along-track and cross-track slopes as follows:

$$170$$

$$171 \quad s_e = \frac{\partial h}{\partial e}, s_n = \frac{\partial h}{\partial n}, s_c = \frac{\partial h}{\partial c}, s_a = \frac{\partial h}{\partial a} \quad (1)$$

172
 173 where s_e , s_n , s_c , and s_a are the slopes in the east, north, along-track, and cross-track
 174 directions, respectively. The grids of longitudes (e) and latitudes (n) are equally spaced at 2 km
 175 intervals in the cross-track (c) and along-track (a) directions. We take the gradient of each of the
 176 longitude and latitude grids to construct unit vectors to project the model east and north slopes
 177 into cross-track and along-track slopes as follows:

$$178$$

$$179 \quad \begin{bmatrix} s_c \\ s_a \end{bmatrix} = \begin{bmatrix} \frac{\partial e}{\partial c} & \frac{\partial n}{\partial c} \\ \frac{\partial e}{\partial a} & \frac{\partial n}{\partial a} \end{bmatrix} \begin{bmatrix} s_e \\ s_n \end{bmatrix} \quad (2)$$

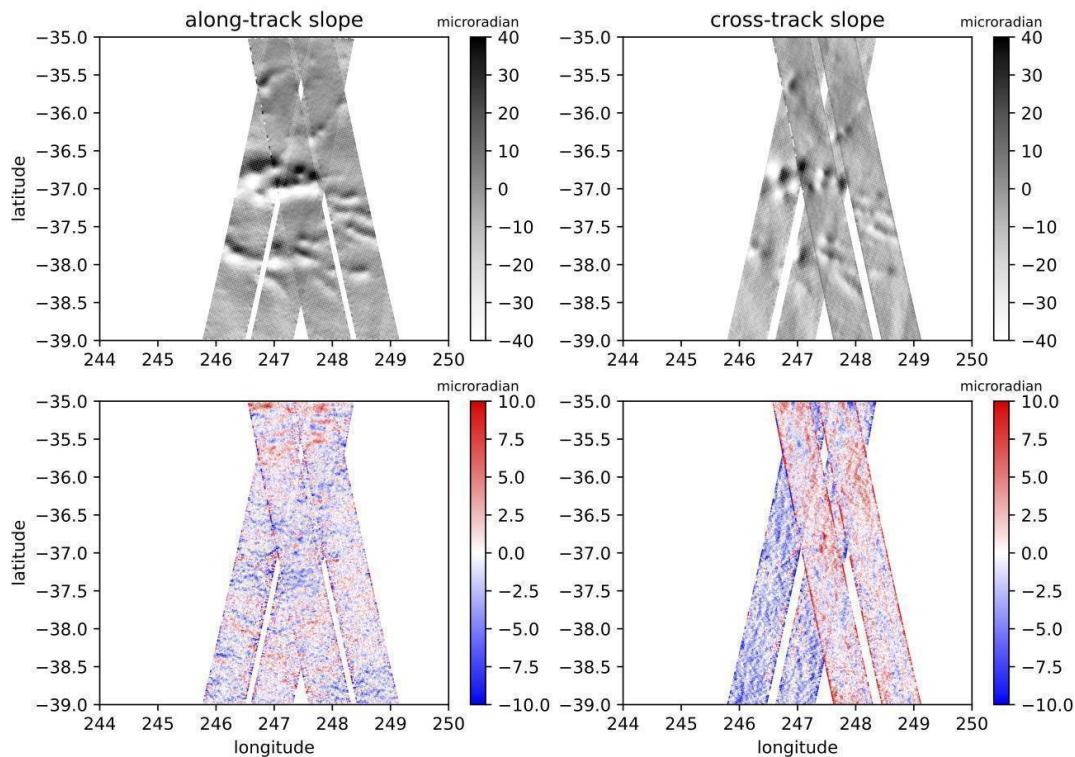
180 where, for example, $\frac{\partial e}{\partial c}$ is the derivative of the east distance in meters (i.e., longitude scaled by
 181 the cosine of the latitude) with respect to the cross-track distance (in meters).

182
 183 The analytical inverse of this 2 by 2 projection matrix is used to convert the SWOT along-
 184 and cross-track slopes into north and east slopes and ultimately gravity anomaly and vertical
 185 gravity gradient. An example of the along-track and cross-track slopes in microradians for
 186 ascending pass 011 and descending pass 026 of cycle 541 (with a typical SWH of 4.0 m) is
 187 shown in Figure 3a,b (no data editing nor crossover correction applied). The gravitational
 188 signatures of the Foundation Seamounts are clearly visible in single passes of SWOT data and
 189 provide the short-wavelength signal for this study.

190
 191 Using equation 2, we project the east and north model slopes shown, in Figure S3, into the
 192 along-track and cross-track directions and subtract them from the SWOT slopes to reveal the
 193 residual slopes (Figure 3c,d). There are several features in these residual slopes worth noting.

194 First the residual slopes have a pervasive short-wavelength noise with amplitude of 2-3 μrad
 195 mainly related to ocean surface waves. The noise has higher amplitude along the edges of the
 196 swaths because the low-pass filter applied on the original SSH has side lobes, and we will edit
 197 using the quality flag later. In addition, the residual cross-track slope from the ascending pass
 198 011 is predominantly negative (blue) with an offset of around -2.5 μrad while the cross-track

199 slope from the descending pass 026 has a slight positive (red) bias. This reflects interferometer
 200 baseline roll error to be removed by the height crossover analysis. The quadratic term in roll
 201 error will bring a slope to the along-/cross-track slope measurement, disrupting real geoid signals
 202 thus not considered in this study. SWOT post-launch evaluation confirms that the error before
 203 calibration is primarily at the larger time scales (Ubelmann et al, in prep). This aligns with the
 204 small along-track slope bias, and the larger cross-track slope bias observed in our study. Note the
 205 SWOT data and the model are completely independent. We have not adjusted the SWOT data
 206 (no crossover correction applied) in any way so our analysis reflects the inherent accuracy of the
 207 L2_LR_SSH product.

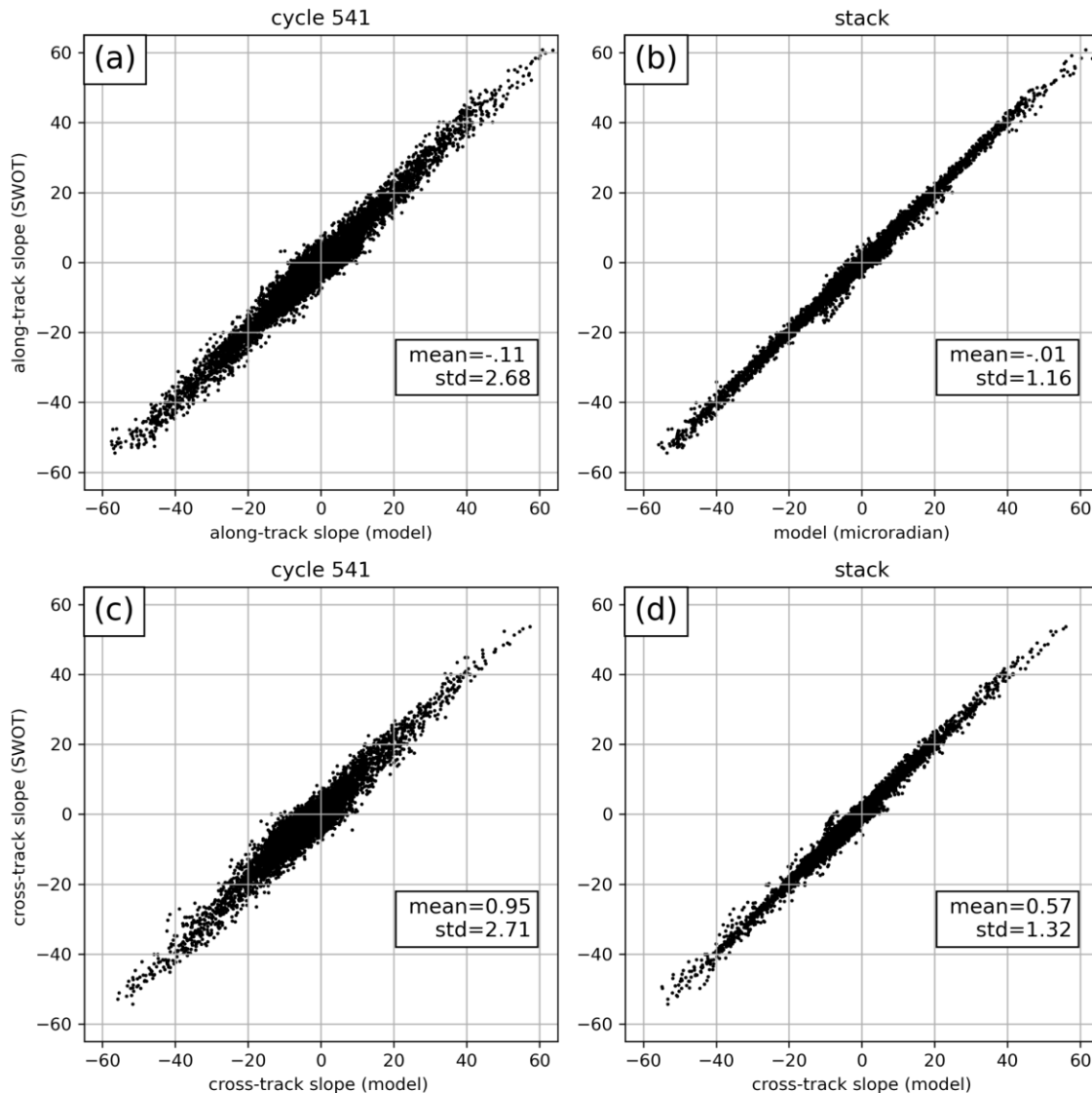


208
 209 **Figure 3.** (a) Along-track and (b) Cross-track slope without crossover correction nor data edits
 210 for one SWOT cycle (541) along ascending (pass 011) and descending (pass 026). (c) Difference
 211 between SWOT along-track slope and model along-track slope shows mainly small spatial scale
 212 noise, with higher noise on the edges of the swaths. (d) Difference between SWOT cross-track
 213 slope and model cross-track slope shows noise but also a mean slope difference of $-2.5 \mu\text{rad}$
 214 (Pass 011) due to uncorrected spacecraft roll error.
 215

216 **3 Accuracy**

217 We now have the components to assess the accuracy and spatial resolution of individual
218 passes of SWOT KaRIn data as well as stacks of data. The analysis is performed on passes 011
219 and 026. We report the pass 011 result in the paper and pass 026 result in the supplement.

220
221 The accuracy of the SWOT data is established through point-wise spatial comparison of
222 along-track and cross-track slopes with the matching model slopes. An example is shown in
223 Figure 4, for one cycle (541) as well as the stack/average of 91 cycles. The along-track slope of
224 the single cycle has a mean of $-0.11 \mu\text{rad}$ and a standard deviation of $2.68 \mu\text{rad}$ while the stack
225 has a smaller mean of $-0.01 \mu\text{rad}$ and standard deviation of $1.16 \mu\text{rad}$. These statistics are better
226 than the comparison of the model gravity with the ship gravity (Figure 2), probably because the
227 ship gravity has some outliers related to sharp turns of the vessel that should be edited. The
228 standard deviation of a single cross-track slope and the stack slope are $2.71 \mu\text{rad}$ and $1.32 \mu\text{rad}$,
229 which is similar to the standard deviation in the along-track direction, for both the single cycle
230 and the stack. However, the mean cross track differences are significantly larger than in the
231 along-track direction, $0.95 \mu\text{rad}$ for cycle 541 and $0.57 \mu\text{rad}$ for the stack. This reflects the
232 residual roll error uncorrected in the current beta pre-validated SWOT KaRIn SSH product. This
233 is a remarkable achievement since $1 \mu\text{rad}$ of orientation error of the 10 m long interferometer
234 baseline corresponds to a height positional error between the antennas of only 10 micrometers!



235

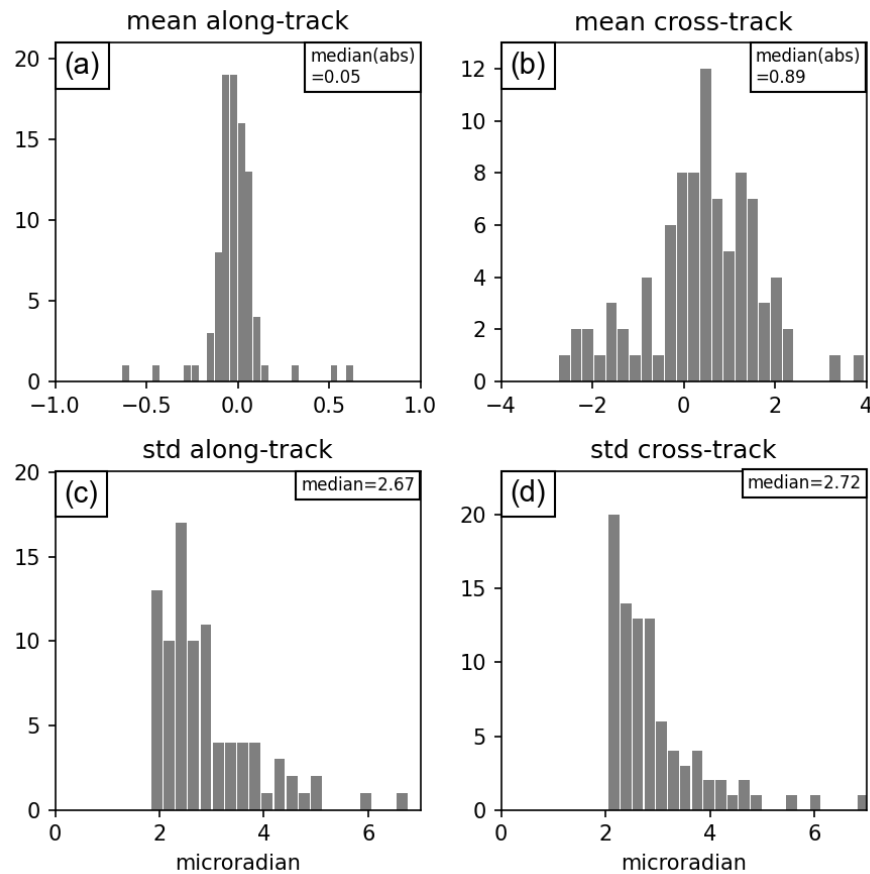
236 **Figure 4.** (a) Along-track slope from SWOT (cycle 541) versus model along track slope in the
 237 unit of μrad . The mean and standard deviation (std) of the difference between SWOT and model
 238 is $-0.11 \mu\text{rad} / 2.68 \mu\text{rad}$. (b) Stacked along-track slope vs model along-track slope. The mean/std
 239 of the difference is $-0.01 \mu\text{rad} / 1.16 \mu\text{rad}$. (c) Cross-track slope from SWOT (cycle 541) versus
 240 model along track slope. The mean/std of the difference is $0.95 \mu\text{rad} / 2.71 \mu\text{rad}$. (d) Stacked
 241 cross-track slope vs model along-track slope. The mean/std of the difference is $0.57 \mu\text{rad} / 1.32$
 242 μrad .

243

244

245 The complete analysis of all 91 repeats of pass 011 are provided in Table S2 with a summary
 246 in Figure 5. We define slope error as the difference between the SWOT slope and model slope.
 247 For each cycle, we can calculate the mean and standard deviation of the slope error. In the along-
 248 track direction, a typical along-track mean slope error is only $0.05 \mu\text{rad}$ for each cycle. This is
 249 based on the median of the absolute value of the mean slope error. In contrast, a typical cross-

250 track mean slope error is much larger, $0.89 \mu\text{rad}$. This is much larger than the model slope error
 251 so will need to be adjusted when processing SWOT KaRIn data for almost any application.



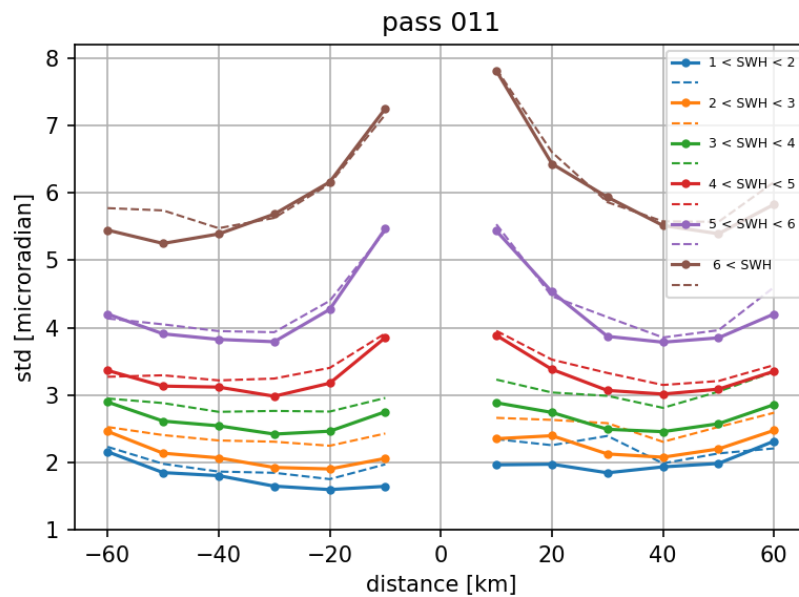
252

253 **Figure 5.** (a) Histogram of the mean difference in along-track slope between the SWOT data and
 254 the model (see Table 1). (b) Same histogram for the cross-track slope has typically large absolute
 255 deviations of $\sim 0.9 \mu\text{rad}$. (c)/(d) Histogram of standard deviation (std) of along/cross-track slope
 256 between the SWOT data and the model.

257

258 The more interesting result is related to the standard deviation of the along-track and cross-
 259 track slope which is typically $2.67 \mu\text{rad}$ and $2.72 \mu\text{rad}$, respectively (see Figure 5c and 5d). The
 260 L2_LR_SSH data on a 2 km grid are low-pass filtered from the original 250 m grid; the filter has
 261 0.5 gain at a wavelength of 4.5 km (Stiles et al., 2023). The main source of noise is related to sea
 262 surface waves and swell which can have wavelengths up to 500 m in the deep ocean. Because
 263 all low-pass filters have side lobes, some of the short (e.g. 500 m) wavelength wave energy can
 264 remain after filtering and decimation. To understand this wave-height noise, we compared the
 265 standard deviation of the slope difference with the significant wave height (SWH) and distance
 266 from the nadir track, both provided with the SWOT L2_LR_SSH data. We divide slope data into
 267 6 groups based on the SWH range and examine the std of slope difference as a function of cross-
 268 track distance from the central nadir (Figure 6). As expected, high slope noise is associated with
 269 high SWH and the along-track slope (solid lines) has slightly lower noise than the cross-track

270 (dashed lines). When the SWH is less than about 3 m, the slope noise is less than about $2.7 \mu\text{rad}$
 271 which is the median noise in a single cycle. As the SWH increases, the noise increases so when
 272 the SWH exceeds 6 m, the noise is typically greater than $5 \mu\text{rad}$ and can be as large as $8 \mu\text{rad}$.
 273 The slope noise also changes with the cross-track distance. When $\text{SWH} < 4 \text{ m}$, noise is highest at
 274 the outer edge of the swath, showing the effect of roll error. While $\text{SWH} > 4 \text{ m}$, noise is the
 275 highest close to the central nadir. This relationship between slope noise and SWH provides a
 276 basis for weighting the contributions to the stack by $1/\text{SWH}$. We performed the same analysis on
 277 descending pass 026, as well using the L3 data (both passes) and the results are similar (see
 278 Tables S2 and S3).



279

280 **Figure 6.** Standard deviation (std) of the difference between 90 cycles of the SWOT slope and
 281 the model slope as a function of SWH and the distance to the Nadir point. Solid lines with dots
 282 are std for the along-track slope difference while dashed lines for the cross-track slope
 283 difference.

284

285 4 Precision

286 The point-wise analysis of the along-track slope (Figure 4 and Table S2) provides the overall
 287 accuracy of the SWOT data. However, there is no information on how the correlation changes
 288 with wavelength or at which wavelength the SWH noise dominates the gravity signal. To address
 289 these questions, we perform spectral and cross-spectral analyses of the SWOT data and the
 290 difference between the SWOT data and the along-track model slope.

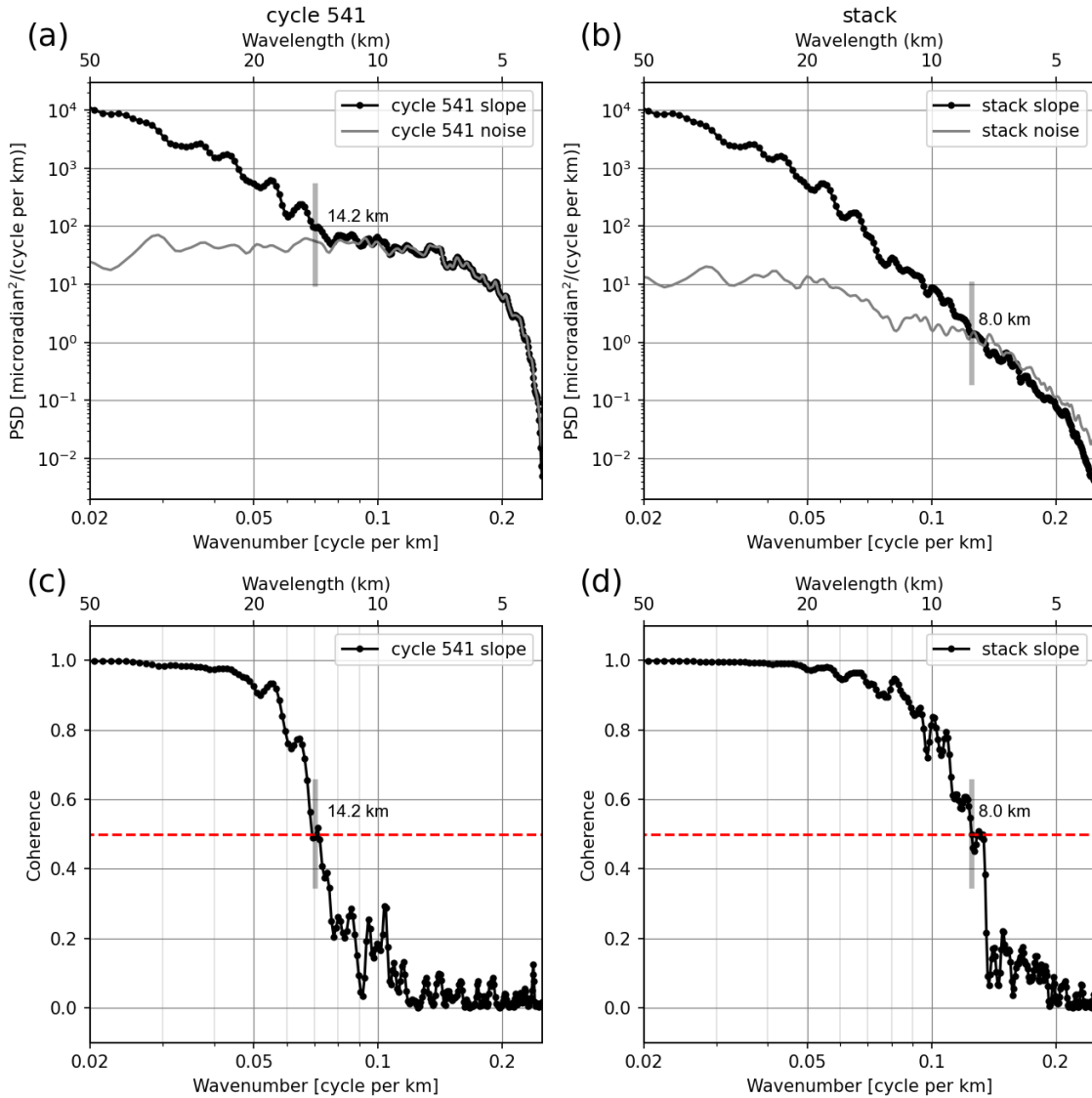
291

292 We show the power spectral density (PSD) of the SWOT along-track slope and its noise from
 293 cycle 541 (Figure 7a) and the stack slope (Figure 7b). The noise is calculated as the difference
 294 between the SWOT along-track slope and the model along-track slope. The stack slope is
 295 constructed using 64 cycles with good data coverage, and $1/\text{SWH}$ as weight since the standard

296 derivation is linearly related to SWH (Figure 6). There are 27 out of 91 cycles not used because
297 of large data gaps. Data associated with high wave height noise ($SWH > 6m$) is excluded from
298 consideration.

299

300 The spatial resolution of the SWOT L2_LR_SSH data is determined by performing a cross-
301 spectral analysis (Bendat and Piersol, 1986) between the along-track slope from SWOT and the
302 model along-track slope. We examine the coherence with the model along-track slope using a
303 single cycle (cycle 541) of SWOT slope (Figure 7c), as well as the SWOT stack slope. SWOT
304 data are edited using the quality flag and each complete column (211 points, denoted by “number
305 of lines” in SWOT L2 data files) of the along-track SWOT and model grids are Hann windowed
306 then zero-padded to 512 points. There are 53 columns (denoted by “number of pixels” in the
307 SWOT L2 data files) without data gaps to compute the coherence using the Welch method. We
308 concatenate the 53 columns and use a 512-point segment length and zero overlap to calculate the
309 cross-spectral coherence between SWOT slope and model slope. The associated 95% confidence
310 level for the squared coherence is 0.028 (Emery and Thompson, 2004). For a single cycle, the
311 coherence drops to 0.5 at around 14.2 km (Figure 7c) where we can also see agreement in energy
312 between the SWOT slope and SWOT slope noise (Figure 7a). A threshold of 0.5 coherence
313 representing equal magnitudes of correlated and uncorrelated components is selected for
314 determining spatial resolution. For the stack slope, SWOT shows a spatial resolution of about 8.0
315 km (Figure 7d), better than the resolution of the current best marine gravity field (~12 km)
316 (Sandwell et al., 2021). There is higher energy in SWOT stack slope noise than stack slope,
317 indicating errors in the MSS model are higher than SWOT stack slope, thus our estimate of 8.0
318 km resolution could be conservative.



319

320 **Figure 7.** (a) Power spectral density (PSD) of along-track slope for cycle 541 (black curve) and
 321 the difference between the SWOT slope and model slope reflects the noise (gray curve). (b) PSD
 322 for stack of 64 cycles for pass 541 (black curve) and the difference between SWOT stack slope
 323 and model slope (grey curve). The power in the stacked slope noise is about 35 times lower than
 324 the individual cycle at a wavelength of 10 km. (c) Cross-spectral coherence between cycle 541
 325 (along-track) and the model falls to 0.5 at a wavelength of 14.2 km. (d) Cross-spectral coherence
 326 between stack (along-track) and the model falls to 0.5 at a wavelength of 8.0 km.

327

328 5 Discussion

329 The swath altimeter aboard SWOT is a radar interferometer that measures height differences
 330 along and across the swath. Like any interferometer, the phase, or height, has a $2N\pi$ ambiguity
 331 that can be resolved using the nadir altimeter or a general knowledge of the MSS height or geoid

332 height. For our applications in marine gravity and bathymetry, knowledge of absolute height is
333 unnecessary; we utilize the derivatives of the geoid including first derivatives such as geoid
334 gradient (i.e., deflections of the vertical) and gravity anomaly, as well as second derivatives such
335 as vertical gravity gradient. Standard nadir altimetry can be used to estimate the MSS height.
336 However, because each profile has long-wavelength errors associated with orbit, atmospheric
337 corrections, tides and other oceanographic effects, it is generally necessary to perform a
338 crossover correction prior to the construction of the MSS (Andersen and Knudsen, 2020;
339 Schaeffer et al., 2023). When the multiple altimeter profiles are gridded, the small cross-track
340 residual height error introduces small-scale noise in the MSS. This noise is significantly reduced
341 by taking the along-track derivative of each profile prior to gridding (Olgiati et al., 1995;
342 Sandwell and Smith, 1997; Yu et al., 2021). Moreover, the derivative operations transform the
343 normally red spectrum of MSS/geoid to something closer to a white spectrum. A significant
344 benefit of this pre-whitening is that it reduces edge effects in any kind of spectral analysis. The
345 downside of taking derivatives of nadir altimeter data is that the short wavelength white noise is
346 transformed to a “blue” noise so a carefully-designed low-pass filter is needed to suppress the
347 noise.

348
349 The best marine gravity anomaly models from nadir altimeters have accuracy of 2-3 mGal
350 and must be low-pass filtered at a wavelength of at least 14 km to suppress the short wavelength
351 noise that has been amplified by taking derivatives. As we demonstrate in this study, this
352 accuracy and resolution is insufficient to assess the quality of the SWOT data so we have used
353 the very high-resolution seafloor bathymetry in the Foundation Seamounts area to improve the
354 accuracy to 1.42 mGal and a resolution of 6.8 km based on a comparison with very high-quality
355 shipboard gravity. Nevertheless, we have no independent dataset to assess whether the tuned-up
356 altimeter-derived gravity is more or less accurate than the ship gravity.

357
358 Our analysis of individual cycles of SWOT data reveals a standard deviation that is typically
359 $2.6 \mu\text{rad}$ and a spatial resolution of 14.2 km. This indicates that a single wide-swath KaRIn
360 altimeter has the capability to produce marine gravity data with a quality comparable to that
361 achieved over 20 years of traditional nadir altimetry, as shown by Sandwell et al. (2021). The
362 standard deviation increases with increasing SWH (Figure 6). The single-cycle SWOT noise has
363 a relatively flat spectrum between wavelengths of 5 km and 50 km where the low-pass filter
364 dominates (Figure 7a). This flat noise spectrum is unlike standard nadir altimetry where the
365 height spectrum is white and the slope spectrum is blue. Therefore, any additional filtering
366 needed to reduce noise should be applied to the SWOT slopes rather than the heights.

367
368 Stacking 64 repeats of SWOT KaRIn SSH improves the standard deviation to $\sim 1.2 \mu\text{rad}$ and
369 consequently increases the spatial resolution to ~ 8 km. After stacking, both the signal and noise
370 have a red spectrum with a slope of $\sim k^{-6}$ (Figure 7b). Note this analysis is based on the
371 comparison of the model vertical deflection grids which are not perfect. Indeed, after stacking,
372 the noise at wavelengths less than 8 km (grey curve) is higher than the SWOT signal (black
373 curve). Since the noise is the difference between the model slope and the SWOT slope, the
374 model noise must be larger than the SWOT noise, suggesting our estimates for the accuracy and
375 resolution of the stacked SWOT slopes are conservative.

376

377 All of these comparisons are performed without performing any kinds of SWOT data
378 adjustments since we focus on the validation and characterization of SWOT, and the original
379 dataset is optimal. We have experimented applying crossover corrections of 1) a 2nd order fit to
380 the wide-swath SSH and 2) removing the mean offset on the along-/cross-track slopes (1st order
381 correction). Compared to removing only the crossover correction supplied with the dataset, both
382 methods make no difference/improvement on the standard deviation of along-track and cross-
383 track slope (accuracy of SWOT KaRIn SSH) and no improvement on the cross-coherence
384 analysis results (spatial resolution of SWOT KaRIn SSH). Instead, it may remove real geoid
385 signals. There are also remaining phase screens from systematic error in interferometric phase in
386 the cross-track slope. However, we find that the mean cross-track slope typically differs from
387 model slope by $0.89 \mu\text{rad}$ and sometimes this mean slope error exceeds $4 \mu\text{rad}$ for an individual
388 cycle of pass 011. This remaining cross-track error, and possible interferometric phase screens
389 that cause $>2^{\text{nd}}$ order variations in cross-track slopes, should be removed prior to construction of
390 improved gravity products (Yu et al., 2021) but the removal method is an area of research and
391 not discussed here. In contrast, the along-track slope mean slope differences are generally much
392 smaller (0.05 rad) than the noise in the stacked slope ($1.16 \mu\text{rad}$).

393
394

395 Pass 026 of SWOT L2 data shows similar or slightly better performance compared to pass
396 011. Pass 026 has a standard deviation that is typically $2.6 \mu\text{rad}$ and a resolution of 13.0 km . The
397 differences with the model slope in the cross-track direction is similar to in the along-track
398 direction (Table S2).

399

400 The L3 SSH data are on the same 2 km by 2 km grids as L2 low-rate data and it is multi-
401 mission calibrated (Dibarboure et al., 2023). For the L3 dataset, we add MSS back to the fully
402 corrected SSH anomaly to get the SSH, then derive along-/cross-track slopes. The result (Table
403 S3) are very similar to those based on L2 over the Foundation Seamounts: 1) for a single cycle, it
404 shows a similar precision of about $2.6 \mu\text{rad}$ and spatial resolution of about 13.0 km ; 2) for the
405 stack of ~ 90 cycles, it shows $1.2 \mu\text{rad}$ in standard deviation and 8 km in spatial resolution. L3
406 datasets are expected to be a significant improvement upon L2 calibration for 1-day orbit regions
407 far away from 1-day crossovers (e.g. near the equator) (Dibarboure et al., 2023). The Foundation
408 Seamounts being exactly on a crossover explains the similarity between L2 and L3 products.
409 When compared with model slopes, we find a slightly larger typical offset in the cross-track
410 direction ($0.12 \mu\text{rad}$) than in the along-track direction ($0.03 \mu\text{rad}$), suggesting that further efforts
411 on crossover error removal are needed.

412

413 One scenario for improving the global marine gravity using 2 km resolution SWOT data is to
414 use a remove-grid-restore method: 1) Remove along-track and cross-track model slopes from the
415 SWOT data using the best available vertical deflection grids based on nadir altimetry. 2) Remove
416 the mean cross-track slope difference over segments of 2000 km . Our analysis does not provide
417 information on how the cross-track slope error varies along the track. 3) Stack the along- and
418 cross-track slopes using a weighting based on the $\sim 1/\text{SWH}$. 4) Project the along- and across-
419 track stacked residual slopes into the east and north directions using the inverse of equation (2).
420 5) Perform a block median of residual east and north slopes and grid them using a spline in
421 tension algorithm such as the GMT *surface* program. There will be diamond-shaped areas having
422 no SWOT coverage so areas further than about 4 km from a SWOT measurement should be

423 padded to zero prior to gridding to suppress spline overshoots. 6) Finally add the model slopes
424 to the gridded residual slopes. At this stage, it is feasible to compute the gravity anomaly or any
425 higher-order derivatives of the gravity field.

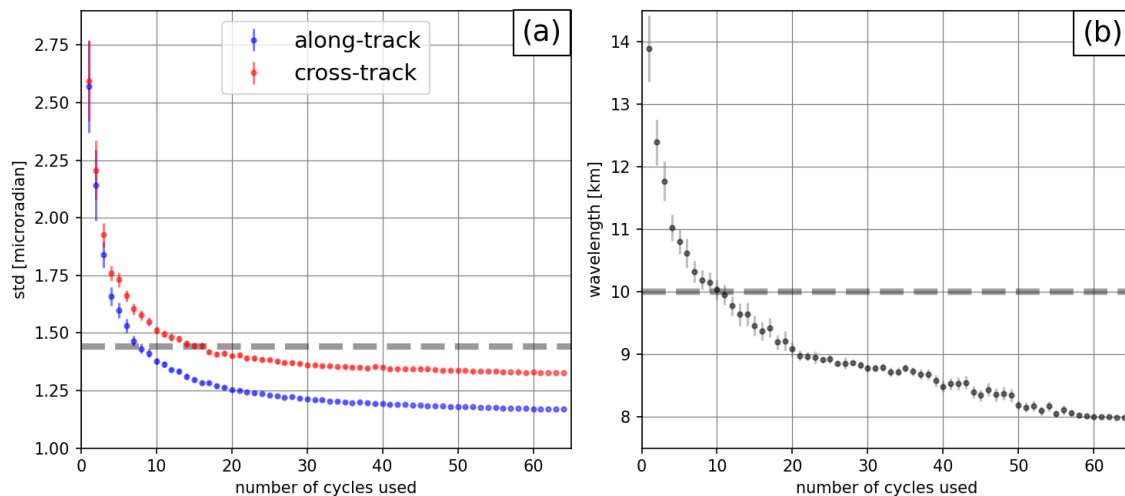
426
427 Our SWOT data evaluation is performed over the Foundation Seamounts where ocean noise is
428 one or two orders of magnitude smaller compared to geoid signals. Nevertheless, our conclusions
429 can also be applied in regions where ocean noise cannot be ignored. SSH anomaly is a zero-
430 centered random process with temporal correlation, it will average to zero almost like noise
431 using many repeats (Dibarboure and Pujol, 2021).

432
433 This entire analysis mainly pertains to the construction of marine gravity products from
434 SWOT although aspects of the processing and analysis are also relevant for extracting small-
435 scale oceanographic signals from SWOT data. One important issue related to marine gravity is
436 that, because of the natural upward continuation low-pass filter, the amplitude of the gravity
437 signal at wavelengths less than the mean ocean depth is vanishingly small. Consider, for
438 example, a 10 mGal amplitude gravity anomaly having a wavelength of 8 km measured just
439 above the seafloor having a depth of 4000 m. Because of Newton's law, the amplitude of this
440 anomaly measured on the sea surface will be attenuated by $\exp\left(-\frac{2\pi z}{\lambda}\right) = 0.043$. The
441 attenuation of this natural low-pass filter is stronger than the low-pass filter used to construct the
442 2 km resolution SWOT ocean product from the 250 m SWOT data (Stiles et al., 2023).
443 Therefore, except in rare cases of shallow ocean (< 400 m in depth) and large amplitude gravity,
444 the 2-km grid supplied with the L2_LR product will be nearly optimal for constructing marine
445 gravity products. In coastal regions, the 250-m grid product is needed and errors related to
446 barotropic tides and internal tides need to be considered carefully.

447
448 Another important result of the natural upward continuation filter is that one can be confident
449 that anomalies having wavelengths less than about 8 km are not caused by residual error in the
450 MSS or SSS models; these anomalies must be true oceanographic signals or noise. It is worth
451 mentioning that parallel studies are concurrently being conducted, focusing on the assessment of
452 SWOT's ability to measure rapidly changing ocean dynamics such as currents, eddies, and waves
453 (Wang et al., in prep). These dynamic elements represent the primary focus of the SWOT
454 mission, even though, for the purposes of this study, they are treated as noise. There are several
455 benefits when working with gradients rather than heights. First, as discussed above, the short-
456 wavelength (< 40 km) noise in the model gradient grids is smaller than the short wavelength
457 noise in the model MSS grids so one can isolate smaller oceanographic signals using slopes
458 rather than heights. In addition, since the slope noise is relatively white having amplitude of ~ 2.5
459 μrad , one can easily estimate the observation threshold amplitude of a shorter wavelength
460 wavelike signal, for example an ocean surface wave with 40 mm amplitude and 4 km wavelength
461 will exceed the slope noise in the 250 m ocean product.

462
463 A final question related to the science part of the SWOT mission is how many repeat cycles
464 will be needed to make a significant improvement in the global marine gravity derived from all
465 nadir altimeters? For pass 011, the standard deviation between the original slope grids using
466 traditional radar altimetry and the improved model grid using shipborne data is $1.50 \mu\text{rad}$ for the
467 east component and $1.44 \mu\text{rad}$ for the north component. We show that by stacking 60+ repeats of
468 SWOT KaRIn data, an accuracy of $1.2 \mu\text{rad}$ and a spatial resolution of 8 km can be achieved

469 (Figures 4b and 8c). For each specific number of cycles used, we bootstrap the 60+ repeats with
 470 50 realizations to obtain the along-/cross-track standard deviation, and the associated 95%
 471 confidence interval, between the SWOT stack and the model stack versus the number in the
 472 stack, as depicted in Figure 8a. The cross-track standard deviation is somewhat higher than the
 473 along-track because of the higher noise on the edges of the swaths as seen in Figure 1d, although
 474 some of the edge noise was removed using the quality flag. If we just consider the stacked along-
 475 track slopes it will take 8 repeat cycles for the accuracy of the SWOT along-track slope to match
 476 the accuracy of the north component of the V32 vertical deflection. In terms of resolution, we
 477 constructed the spatial resolution versus the number of cycles used (Figure 8b) using similar
 478 methods as for the standard deviation. It will take 11 cycles for the SWOT vertical deflection to
 479 match the 10-km resolution of the V32 vertical deflection. After about 20 repeat cycles, the
 480 SWOT gravity field will be significantly better than the current gravity models based on nadir
 481 altimetry. Note it has taken 232 months of nadir geodetic mission data to achieve the accuracy
 482 of the current models so a significant improvement in just 14 months is a major achievement.
 483 This is certainly a conservative estimate because some fraction of the standard deviation between
 484 the stacked SWOT slopes and the model slopes is due to remaining error in the model and the
 485 magnitude of this error is largely unknown.



486

487 **Figure 8.** (a) Standard deviation of the difference between along-/cross-track SWOT stacked
 488 slopes and the model slope versus the number of cycles used in the stack. (b) Spatial resolution
 489 of along-track slope (coherence 0.5) versus number of cycles in the stack. The end members for
 490 1 cycle and 64 cycles are shown in Figures 4 and 7. Grey dashed lines are the current accuracy
 491 (a) and resolution (b) of the V32 altimeter-only model. Error bars show the 95% confidence
 492 interval. Improvements from SWOT will require ~11 repeat cycles in the 21-day science orbit.

493

494 6 Conclusions

- 495 • The Foundation Seamounts area provides a unique opportunity to assess the accuracy and
 496 resolution of the marine gravity field that will be recovered by SWOT. The area has
 497 complete multibeam coverage and highly-accurate shipboard gravity profiles to construct

- 498 east and north grids of deflection of the vertical for comparison with along-/cross-track
499 sea surface gradients measured by SWOT.
- 500 ● A single cycle of SWOT coverage, at a typical SWH of 4 m, has a precision of 2.6 μrad
501 and a spatial resolution of 13 km. The mean along-track slope is commonly within 0.05
502 μrad of the model slope while the mean cross track slope error is somewhat larger ~ 0.9
503 μrad - 2.0 μrad due to the remaining roll error. The mean cross-track slope from SWOT
504 should be adjusted to the model slope before constructing marine gravity.
 - 505 ● The slope noise increases significantly for SWH above 5 m so cycles should be weighted
506 by $\sim 1/\text{SWH}$ during stacking.
 - 507 ● A stack of ~ 60 cycles of SWOT data provides a dramatic improvement in precision ~ 1.2
508 μrad and spatial resolution ~ 8 km. This dramatic increase in accuracy and, especially
509 resolution, would reveal much more detail in small-scale seafloor structures such as
510 seamounts and abyssal hills.
 - 511 ● The accuracy and resolution of the marine gravity field derived from SWOT will exceed
512 the accuracy of the current models after 11 repeat cycles (~ 8 months). Significant
513 increases will require about 20 repeat cycles (~ 14 months).
 - 514 ● The optimal method for improving the gravity field from SWOT data will use sea
515 surface gradients projected into the north and east directions and combined with existing
516 models using a standard remove-grid-restore method.

517 **Acknowledgments**

518 This work was supported by the NASA SWOT program (80NSSC20K1138), the Office of Naval
519 Research (N00014-17-1-2866), and the Eric and Wendy Schmidt AI in Science postdoc
520 fellowship. A portion of this work was performed at the Jet Propulsion Laboratory, California
521 Institute of Technology, under contract with NASA. Government sponsorship acknowledged.
522 The Generic Mapping Tools (GMT) (Wessel et al., 2019) were extensively used in data
523 processing. We appreciate efforts from everyone working on the SWOT mission.
524

525 **Data Availability Statement**

526 The data used in this study are accessible to the public. The SWOT L2 KaRIn low rate sea
527 surface height data used in this study is available on EarthData:

528 [https://search.earthdata.nasa.gov/search/granules?p=C2746459620-
529 POCLOUD&pg\[0\]\[v\]=f&pg\[0\]\[gsk\]=-start_date&q=SWOT&tl=1705028636.95513!!](https://search.earthdata.nasa.gov/search/granules?p=C2746459620-POCLOUD&pg[0][v]=f&pg[0][gsk]=-start_date&q=SWOT&tl=1705028636.95513!!)

530 The SWOT L3 low rate data used in this study is available on aviso:

531 [https://www.aviso.altimetry.fr/en/data/products/sea-surface-height-products/global/swot-13-
532 ocean-products.html](https://www.aviso.altimetry.fr/en/data/products/sea-surface-height-products/global/swot-13-ocean-products.html)

533 The east-/north-slopes constructed using nadir altimetry and ship measurements in the
534 Foundation Seamounts, the SIO V32 mean sea surface, and the CLS 2021 mean dynamic
535 topography model are available on zenodo: <https://doi.org/10.5281/zenodo.10494740>
536

537 **References**

538 Andersen, O. B., & Knudsen, P. (2020). The DTU17 global marine gravity field: First validation
539 results. In *Fiducial Reference Measurements for Altimetry: Proceedings of the International*
540 *Review Workshop on Satellite Altimetry Cal/Val Activities and Applications* (pp. 83-87).
541 Springer International Publishing.

542 Bendat, J. G. and A. G. Piersol, (1986) *Random Data Analysis and Measurement Procedures*,
543 2nd ed. New York: Wiley.

544 Dibarboure, G., & Pujol, M. I., (2021). Improving the quality of Sentinel-3A data with a hybrid
545 mean sea surface model, and implications for Sentinel-3B and SWOT. *Advances in Space*
546 *Research*, 68(2), 1116-1139.

547 Dibarboure, G., Ubelmann, C., Flamant, B., Briol, F., Peral, E., Bracher, G., Vergara, O.,
548 Faugère, Y., Soulat, F. and Picot, N., (2022). Data-Driven Calibration Algorithm and Pre-Launch
549 Performance Simulations for the SWOT Mission. *Remote Sensing*, 14(23), p.6070.

550 Dibarboure, G., Ubelmann, C., Faugère, Y., Delepouille, A., Broil, F., Chevrier R. Busche, C.,
551 Treboutte, A., Prandi, P., (2023). SWOT Level-3 Overview: Algorithms and Examples. SWOT
552 Science Team Meeting 2023.
553 https://swotst.aviso.altimetry.fr/fileadmin/user_upload/SWOTST2023/postersPI/faugere_ocean_1
554 [3_PIproject.pdf](#)

555 Devey, C.W., Hékinian, R., Ackermann, D., Binard, N., Francke, B., Hémond, C., Kapsimalis,
556 V., Lorenc, S., Maia, M., Möller, H. and Perrot, K., (1997). The Foundation Seamount Chain: a
557 first survey and sampling. *Marine geology*, 137(3-4), pp.191-200.

558 Thomson, R. E., & Emery, W. J. (2014). *Data analysis methods in physical oceanography*.
559 Newnes.

560 Fu, L.L., Alsdorf, D., Rodriguez, E., Morrow, R., Mognard, N., Lambin, J., Vaze, P. and Lafon,
561 T.,(2009) The SWOT (Surface Water and Ocean Topography) mission: Spaceborne radar
562 interferometry for oceanographic and hydrological applications. *Proceedings of OCEANOBS*, 9,
563 pp.21-25.

564 JPL Internal Document, 2018 : Surface Water and Ocean Topography Mission (SWOT) Project
565 Science Requirements Document, JPL D-61923, Rev. B

566 Maia, M., & Arkani-Hamed, J. (2002). The support mechanism of the young Foundation
567 Seamounts inferred from bathymetry and gravity. *Geophysical Journal International*, 149(1),
568 190-210.

569 Mammerickx, J. (1992). The Foundation Seamounts: tectonic setting of a newly discovered
570 seamount chain in the South Pacific. *Earth and planetary science letters*, 113(3), 293-306.

571 Morrow, R., Fu, L. L., Arduin, F., Benkiran, M., Chapron, B., Cosme, E., d'Ovidio, F., Farrar,
572 J.T., Gille, S.T., Lapeyre, G., Le Traon, P., Pascual, A., Ponte, A., Qiu, B., Rasclé, N.,
573 Ubelmann, C., Wang, J., & Zaron, E. D. (2019). Global observations of fine-scale ocean surface
574 topography with the surface water and ocean topography (SWOT) mission. *Frontiers in Marine*
575 *Science*, 6, 232.

576 Olgiati, A., Balmino, G., Sarrailh, M., & Green, C. M. (1995). Gravity anomalies from satellite
577 altimetry: comparison between computation via geoid heights and via deflections of the vertical.
578 *Bulletin géodésique*, 69, 252-260.

579 Parker, R. L. (1973). The rapid calculation of potential anomalies. *Geophysical Journal*
580 *International*, 31(4), 447-455.

581 Pavlis, N. K., Holmes, S. A., Kenyon, S. C., & Factor, J. K. (2012). The development and
582 evaluation of the Earth Gravitational Model 2008 (EGM2008). *Journal of geophysical research:*
583 *Solid Earth*, 117(B4).

584 Sandwell, D. T., & Smith, W. H. (1997). Marine gravity anomaly from Geosat and ERS 1
585 satellite altimetry. *Journal of Geophysical Research: Solid Earth*, 102(B5), 10039-10054.

586 Sandwell, D. T., Harper, H., Tozer, B., & Smith, W. H. (2021). Gravity field recovery from
587 geodetic altimeter missions. *Advances in Space Research*, 68(2), 1059-1072.

588 Sandwell, D. T., Harper, H., Tozer, B., & Smith, W. H. (2021). Gravity field recovery from
589 geodetic altimeter missions. *Advances in Space Research*, 68(2), 1059-1072.

590 Sandwell, D., Yu, Y., Schaeffer, P., Pujol, I., Dibarboure, G., & Wang, J. SWOT MSS Removal.
591 github.

592 Schaeffer, P., Pujol, M. I., Veillard, P., Faugere, Y., Dagneaux, Q., Dibarboure, G., & Picot, N.
593 (2023). The CNES CLS 2022 Mean Sea Surface: Short Wavelength Improvements from
594 CryoSat-2 and SARAL/AltiKa High-Sampled Altimeter Data. *Remote Sensing*, 15(11), 2910.

595 Stiles, B., P. Dubois, C.Chen, A. Bohe, L. Fu, R. Morrow (2023). Surface Water and Ocean
596 Topography Project Algorithm Theoretical Basis Document Long Name: Level 2 KaRIn Low
597 Rate Sea Surface Height Science Algorithm, California Institute of Technology, NASA Jet
598 Propulsion Lab, 88 pp. [https://podaac.jpl.nasa.gov/swot?tab=datasets-](https://podaac.jpl.nasa.gov/swot?tab=datasets-information§ions=about%2Bdata%2Bnews%2Bresources)
599 [information§ions=about%2Bdata%2Bnews%2Bresources](https://podaac.jpl.nasa.gov/swot?tab=datasets-information§ions=about%2Bdata%2Bnews%2Bresources)

600 Surface Water Ocean Topography (SWOT). 2017. Mission performance and Error budget, JPL
601 internal document, JPL D-79084,
602 [https://swot.jpl.nasa.gov/system/documents/files/2178_2178_SWOT_D-](https://swot.jpl.nasa.gov/system/documents/files/2178_2178_SWOT_D-79084_v10Y_FINAL_REVA__06082017.pdf)
603 [79084_v10Y_FINAL_REVA__06082017.pdf](https://swot.jpl.nasa.gov/system/documents/files/2178_2178_SWOT_D-79084_v10Y_FINAL_REVA__06082017.pdf)

604 Surface Water Ocean Topography (SWOT). 2023a. SWOT Level 2 KaRIn Low Rate Sea
605 Surface Height Data Product, Version 1.1. Ver. 1.1. PO.DAAC, CA, USA. Dataset accessed
606 [2023-09-30] at <https://doi.org/10.5067/SWOT-SSH-1.1>

607 Surface Water Ocean Topography (SWOT), 2023b. SWOT product description
608 L2_LR_SSH_20220902 RevA, [https://archive.podaac.earthdata.nasa.gov/podaac-ops-cumulus-](https://archive.podaac.earthdata.nasa.gov/podaac-ops-cumulus-docs/web-misc/swot_mission_docs/pdd/D-56407_SWOT_Product_Description_L2_LR_SSH_20220902_RevA.pdf)
609 [docs/web-misc/swot_mission_docs/pdd/D-](https://archive.podaac.earthdata.nasa.gov/podaac-ops-cumulus-docs/web-misc/swot_mission_docs/pdd/D-56407_SWOT_Product_Description_L2_LR_SSH_20220902_RevA.pdf)
610 [56407_SWOT_Product_Description_L2_LR_SSH_20220902_RevA.pdf](https://archive.podaac.earthdata.nasa.gov/podaac-ops-cumulus-docs/web-misc/swot_mission_docs/pdd/D-56407_SWOT_Product_Description_L2_LR_SSH_20220902_RevA.pdf)

611 Surface Water Ocean Topography (SWOT). 2017, Mission performance and Error budget, JPL
612 internal document, JPL D-79084

613 Tozer, B., Sandwell, D. T., Smith, W. H., Olson, C., Beale, J. R., & Wessel, P. (2019). Global
614 bathymetry and topography at 15 arc sec: SRTM15+. *Earth and Space Science*, 6(10), 1847-
615 1864.

616 Wang et al. (2024): Performance of the SWOT Ka-band Radar Interferometer 100 km
617 wavelength, in-prep, *GRL*

618 Watts, A. B. (2001). *Isostasy and Flexure of the Lithosphere*. Cambridge University Press.

619 Wessel, P., & Bercovici, D. (1998). Interpolation with splines in tension: a Green's function
620 approach. *Mathematical Geology*, 30, 77-93.

621 Wessel, P., Luis, J. F., Uieda, L., Scharroo, R., Wobbe, F., Smith, W. H., & Tian, D. (2019). The
622 generic mapping tools version 6. *Geochemistry, Geophysics, Geosystems*, 20(11), 5556-5566.

623 Yu, D., Hwang, C., Andersen, O. B., Chang, E. T., & Gaultier, L. (2021). Gravity recovery from
624 SWOT altimetry using geoid height and geoid gradient. *Remote Sensing of Environment*, 265,
625 112650.

626 Yu, Y., Sandwell, D. T., & Gille, S. T. (2023). Seasonality of the Sub-Mesoscale to Mesoscale
627 Sea Surface Variability From Multi-Year Satellite Altimetry. *Journal of Geophysical Research:*
628 *Oceans*, 128(2), e2022JC019486.